

# 3D Laser Scribed Graphene Derived from Carbon Nanospheres: An Ultrahigh-Power Electrode for Supercapacitors

Wenli Zhang, Yongjiu Lei, Qiu Jiang, Fangwang Ming, Pedro M. F. J. Costa, and Husam N. Alshareef\*

Laser scribed graphene (LSG) electrodes hold great potential as supercapacitor electrodes. However, the rate performance of LSGs has been limited by the micropore-dominated electrode structure. Here, a new method is proposed to prepare LSG electrodes with a 3D porous framework dominated by meso- and macro-pores, a property that enables exceptional rate performance. The process uses amorphous carbon nanospheres (CNS) as precursors, which, after laser scribing, are transformed into highly turbostratic graphitic carbon electrodes (henceforth denoted as CNS-LSG) with a 3D framework structure dominated by meso- and macro-pores. When used as electrodes in conventional supercapacitor devices, the CNS-LSG electrodes exhibit a high volumetric power density of  $28 \text{ W cm}^{-3}$ , which is 28 times higher than that of current commercial activated carbon supercapacitors, and is the highest among all the reported laser scribed/induced graphene electrodes.

Supercapacitors fill the energy-power void between rechargeable batteries and aluminum electrolytic capacitors.<sup>[1,2]</sup> However, the energy densities and power densities of supercapacitors cannot cover the entire gap between rechargeable battery and aluminum electrolytic capacitors. In this regard, the development of supercapacitors has two principal directions. One direction is developing supercapacitors with high energy density for long-term energy storage applications,<sup>[3,4]</sup> such as electric vehicles, and renewable energy storage. The other direction is developing high-power supercapacitor which bridges the gap between commercial activated carbon (AC) supercapacitor and aluminum electrolytic capacitor. In fact, high-power supercapacitors serve an important role as they can be used in frequency regulation of intermittent renewable-energy-supported electrical grids and electronic circuits.<sup>[5]</sup>

Dr. W. Zhang, Y. Lei, Q. Jiang, F. Ming, Prof. P. M. F. J. Costa, Prof. H. N. Alshareef  
Materials Science and Engineering  
Physical Science and Engineering Division  
King Abdullah University of Science and Technology (KAUST)  
Thuwal 23955-6900, Saudi Arabia  
E-mail: husam.alshareef@kaust.edu.sa

The ORCID identification number(s) for the author(s) of this article can be found under <https://doi.org/10.1002/smt.201900005>.

DOI: 10.1002/smt.201900005

Offering high conductivity and short ion diffusion distances, graphene-based electrode materials are promising candidates for high-power supercapacitors.<sup>[6–9]</sup> Unfortunately, due to the relatively complicated preparation and assembly process of graphene electrodes, their use has been limited.<sup>[10,11]</sup> So, simple, low-cost preparation methods (with potential for scale-up) for the fabrication of graphene-based electrodes need to be developed. In this respect, hydrothermally produced carbons (HPC), as a family of biomass-derived amorphous carbon,<sup>[12]</sup> are particularly well-suited to become active materials in supercapacitors since HPC can be prepared from abundant renewable natural sources containing appropriate building-block molecules, such as glucose, cellulose, starch, and lignin.<sup>[13–15]</sup> Still, the non-

porous texture, high oxygen content, and low conductivity of the as-prepared HPCs continue to impair its application in energy storage systems. For this reason, additional steps have been considered to enhance the porosity of HPC which include chemical activation,<sup>[14,16]</sup> template-directed carbonization,<sup>[17]</sup> and self-activation.<sup>[18]</sup> Besides porosity, the elimination of oxygen and re-structuring of the carbon lattice needs to be looked into. Few HPC-related reports have focused on this issue.

Although high-temperature treatment induces the graphitization of carbon precursors having a fair degree of lattice alignment (soft carbon),<sup>[19]</sup> the high-temperature treatment of amorphous carbon would only result in hard carbon, unless catalysis or high pressure is applied.<sup>[20–23]</sup> There is great interest to develop simple, catalysis-free and low-temperature graphitization methods, such as electrochemical graphitization,<sup>[24,25]</sup> and laser scribing graphitization.<sup>[26–28]</sup> Laser scribing is a direct-write method that can be used to convert graphene oxide, polyimide and many kinds of commercial polymers to porous graphene films which can be directly used as binder-free electrodes for supercapacitors.<sup>[26,28–30]</sup> Laser scribing preparation of graphene is a simple, catalyst-free, eco-friendly method, and shows great potential toward electronics and energy storage devices.<sup>[31]</sup> If HPCs from various natural biomass were used to prepare LSG electrodes, we can open a sustainable route for the conversion of biomass to porous graphene.

In this article, hydrothermally produced carbon nanospheres (CNS) are directly transformed into 3D porous graphene

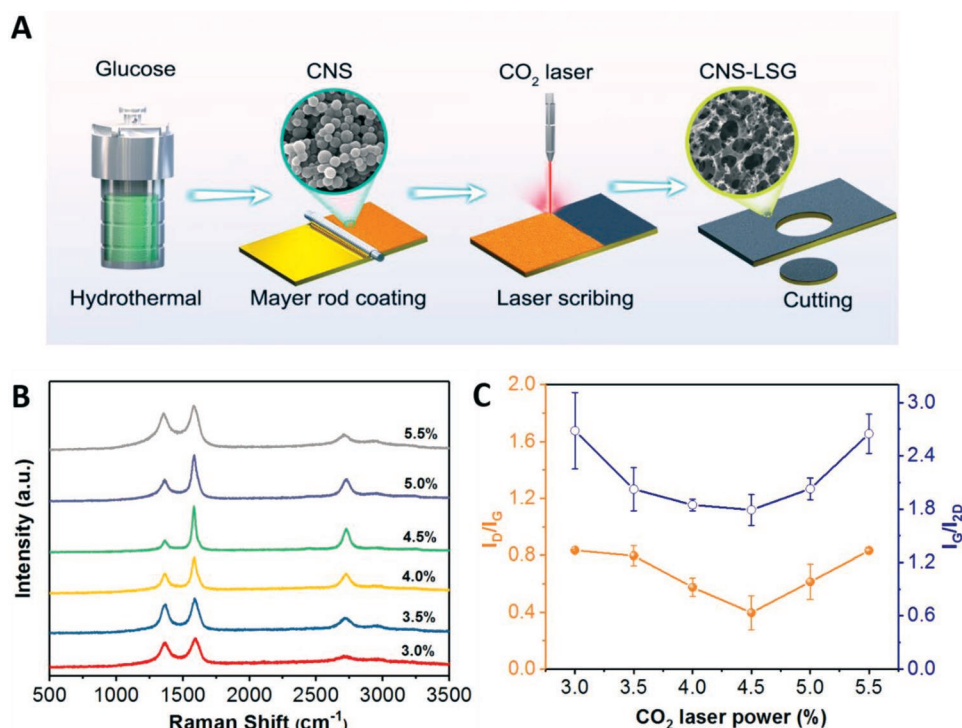


**Figure 1.** A) The schematic diagram of the laser scribing fabrication of CNS-LSG electrode; B) the Raman spectra of CNS-LSG electrodes prepared at different applied CO<sub>2</sub> laser power; and C) the dependence of  $I_D/I_G$  and  $I_G/I_{2D}$  ratios on the applied CO<sub>2</sub> laser power.

electrode through a one-step CO<sub>2</sub> laser scribing process. The obtained laser scribed graphene (LSG) electrode (henceforth referred to as CNS-LSG) possesses 3D hierarchical porous structure dominated by meso- and macro-pores. The symmetric supercapacitors assembled using CNS-LSG electrodes exhibit ultrahigh volumetric power density, high-frequency response, and long cycle life. The greatly improved power performance and the simple preparation of CNS-LSG could enable it to compete with traditional aluminum electrolytic capacitors in a number of applications. Hence, this article opens an avenue for preparing 3D porous graphene from various biomasses for high-power supercapacitor application.

The detailed fabrication processes of the CNS-LSG electrodes is illustrated in Figure 1A. The CNS was obtained using a hydrothermal reaction, which is a well-developed method for the preparation of CNS with numerous carboxylates and hydroxyl groups from various biomasses.<sup>[32–34]</sup> The CNS powders were mixed with sodium carboxymethyl cellulose (CMC) binders to make a film on gold-coated aluminum substrate using a Mayer rod coating technique. Upon drying, the CNS film was then irradiated with a CO<sub>2</sub> laser to obtain 3D CNS-LSG electrode films. The 10.6  $\mu\text{m}$  CO<sub>2</sub> laser was chosen due to its ability to convert sp<sup>3</sup> C–C to sp<sup>2</sup> C=C carbon bonds, since the sp<sup>3</sup> C–C has strong absorbance of infrared light in the wave numbers from 700 to 1200 cm<sup>-1</sup> (see Figure S1, Supporting Information). The ablation of sp<sup>3</sup> C–C would create numerous graphene quantum dots which assemble into long-range ordered graphene layers in LSG. After laser scribing, the CNS-LSG was directly used as electrode in symmetric supercapacitors. The influence of laser power on the structure of the CNS-LSG electrode was studied with Raman spectroscopy

(Figure 1B) with varying laser power ranging from 3.0% to 5.5%, with 0.5% increment. The Raman spectra show three main peaks: G peak around 1580 cm<sup>-1</sup> which is commonly assigned to graphitic carbon, D peak around 1350 cm<sup>-1</sup> which results from lattice defects and 2D peak an overtone generally present at 2700 cm<sup>-1</sup>.<sup>[35]</sup> The presence of the 2D peak is evidence for the formation of stacked layers of graphene.<sup>[36]</sup> With increasing laser power from 3.0% to 5.5%,  $I_D/I_G$  ratio decreases first and reaches a minimum of 0.398 at the laser power of 4.5% (Figure 1C). When laser power increases from 5.0% to 5.5%, the  $I_D/I_G$  ratio increases, which suggests that at these high powers, the CNS-LSG is destroyed by laser. Similar  $I_D/I_G$  trends with laser power have been reported for LSG derived from polyimide.<sup>[35]</sup> The minimum  $I_D/I_G$  ratio means that graphene size along the *a* axis is maximized (estimated  $L_a$  of  $\approx 30$  nm, Figure S2, Supporting Information). In addition to the  $I_D/I_G$  ratio, comparing the intensities of the G and 2D peaks can also provide key structural insights. The  $I_G/I_{2D}$  ratio reaches the minimal of 1.79 at the laser power of 4.5%, which indicates that the CNS-LSG was better structured, closer to the spectral signature of multilayered graphene.<sup>[30,37]</sup> We thus conclude that to get good quality 3D graphene from CNS, the laser power should be set at the optimized laser power of 4.5%. In the following discussion, the CNS-LSG electrodes were prepared using a laser power of 4.5%, unless otherwise specified.

Laser scribing greatly changes the morphology and structure of CNS. The CNS itself shows spherical morphology, as shown in the scanning electron microscopy (SEM) image in Figure 2A. The CNS can be assembled into a good quality film using Mayer rod casting with the help of CMC binders (Figure 2B).

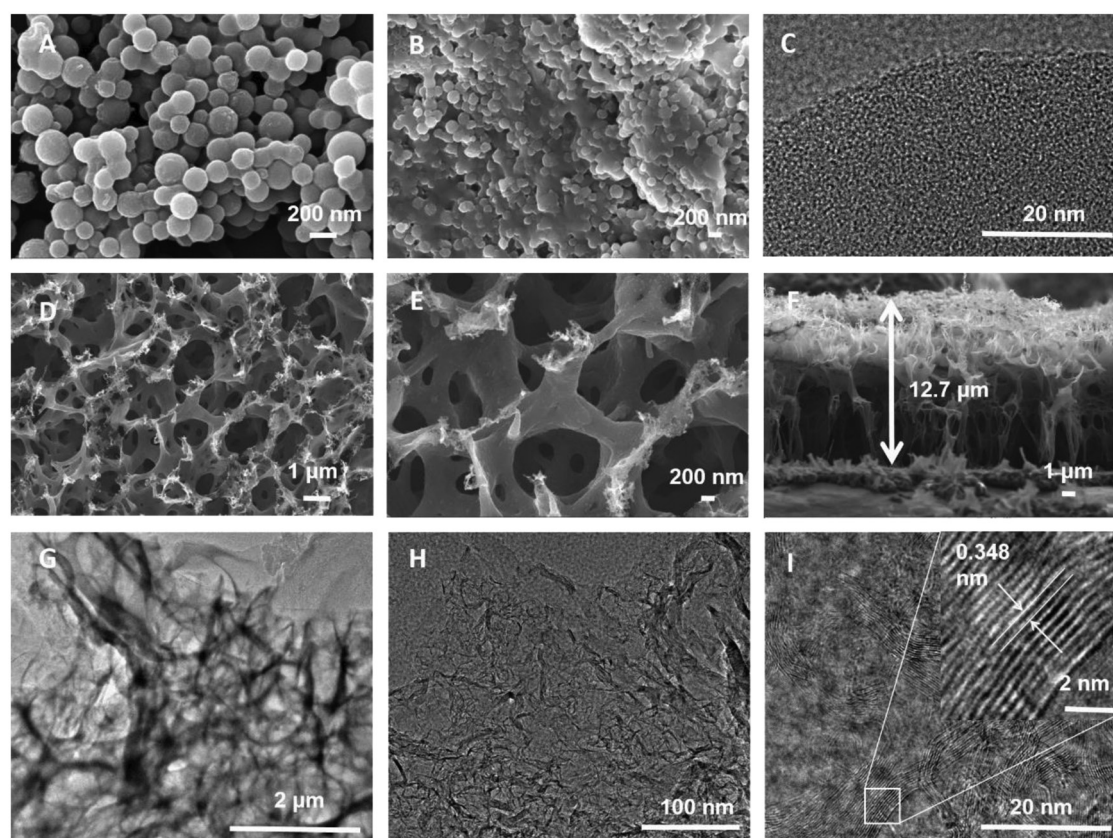


**Figure 2.** A) The SEM image of CNS; B) the SEM image of CNS film on gold-coated aluminum substrate; C) the HRTEM image of CNS; D,E) the SEM images of CNS-LSG; F) the cross-sectional SEM image of CNS-LSG; G) TEM image of CNS-LSG; and H,I) the HRTEM images of CNS-LSG.

The CNS film cannot be used as the electrode for supercapacitors, since the CNS is highly amorphous (Figure 2C), oxygen-rich and has low specific surface area. After laser scribing, the morphology of CNS-LSG film was greatly changed, depending on laser power. At a laser power of 3.0%, the CNS-LSG film did not transform into a good carbon framework, as some CNSs can be seen in Figure S3A,B in the Supporting Information. When the laser power was increased to 3.5% and 4.0%, most carbon nanospheres were transformed into 3D carbon framework (Figure S3C–F, Supporting Information). At a laser power of 4.5%, the CNS-LSG electrode shows uniform 3D carbon framework (Figure 2D,E). It is interesting that the spherical morphology of CNS totally disappeared, and a well-interconnected, 3D carbon framework was formed (Figure S3G,H, Supporting Information). Consistent with the Raman analysis, the SEM images show that a laser power of 4.5% is the optimal power for the preparation of 3D graphene from CNS. Higher powers (>5.0%) destroy the surface of the carbon framework (Figure S3I–L, Supporting Information).

The cross-sectional SEM image of CNS-LSG electrodes shows that the CNS-LSG electrode is macroporous from the top surface to CNS-LSG/substrate interface, with a thickness of about 13  $\mu\text{m}$  (Figure 2F). Cross-sectional SEM image and the low-resolution transmission electron microscopy (TEM) image of CNS-LSG (Figure 2G) both confirm the existence of 3D porous framework structure. High-resolution TEM (HRTEM) image of CNS-LSG shows graphene ribbons in the carbon

matrix (Figure 2H) with a lattice space of 0.348 nm (Figure 2I) corresponding to (002) interlayer spacing. As discussed above, the CNS-LSG electrode is a 3D well-interconnected carbon framework. The 3D macroporous structure of CNS-LSG electrode could enhance the electrolyte diffusion and the graphene layers could enhance the electron conduction, which could render CNS-LSG suitable as electrodes for high power supercapacitors.

As the data above showed, the amorphous CNS was transformed to graphitic carbon after laser scribing. The X-Ray Diffraction (XRD) pattern of CNS-LSG shows a typical peak at  $25.9^\circ$  (Figure 3A) corresponding to (200) interlayer spacing of 0.344 nm, as calculated by the Bragg equation, in accordance with the results from HRTEM.

Whilst electron microscopy identified the presence of macropores, a more detailed analysis of the porosity of CNS-LSG is required.  $\text{N}_2$  adsorption–desorption measurement demonstrates that after the laser scribing process, the Brunauer–Emmett–Teller (BET) surface area increases from  $14.6 \text{ m}^2 \text{ g}^{-1}$  for CNS to the  $87.8 \text{ m}^2 \text{ g}^{-1}$  of CNS-LSG (Figure 3B). Similarly, like CNS, the pore size of CNS-LSG is dominated by meso/macropores (Figure S4, Supporting Information). Different from the LSG derived from polyimide ( $340 \text{ m}^2 \text{ g}^{-1}$ )<sup>[35]</sup> and carbon quantum dots ( $230 \text{ m}^2 \text{ g}^{-1}$ )<sup>[38]</sup> CNS-LSG shows smaller BET surface area and much larger pore size, which is good for electrolyte diffusion and high-power performance supercapacitors.



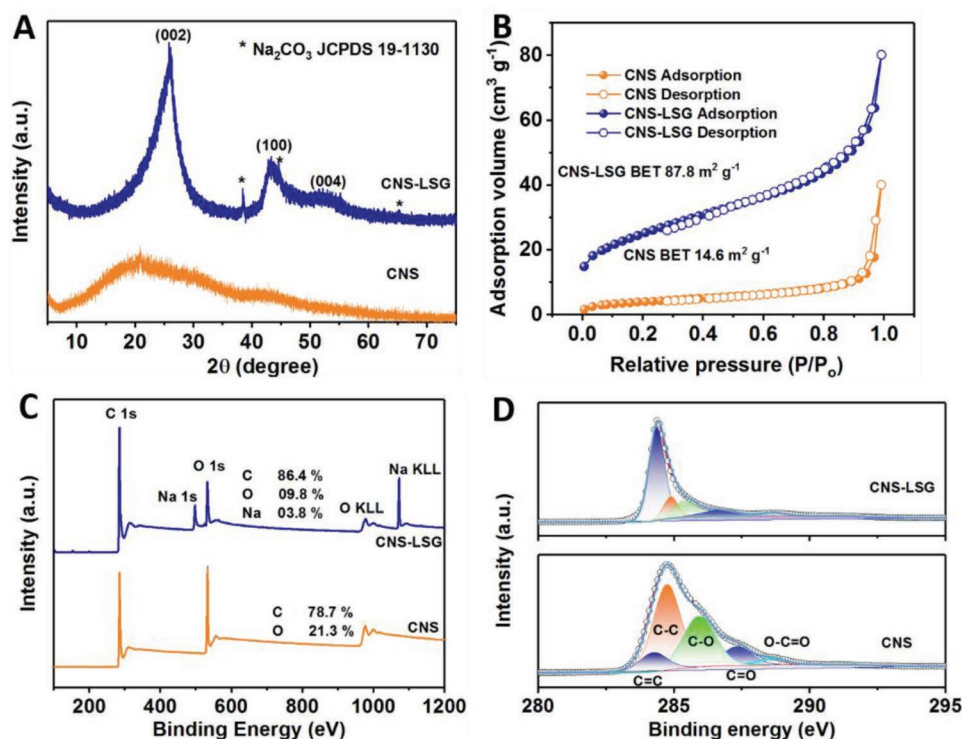


**Figure 3.** A) The XRD patterns of CNS-LSG and CNS; B) the  $N_2$  adsorption and desorption isotherms of CNS-LSG and CNS; C) XPS survey spectra of CNS and CNS-LSG; and D) the C 1s high resolution XPS spectra and the fitting curves of CNS and CNS-LSG.

The presence of moieties such as oxygen-containing functional groups is known to influence the capacitance of carbon materials. Therefore, besides the structure, morphology and porosity, it was also important to understand the surface chemistry of the CNS-LSG material. X-ray photoelectron spectroscopy (XPS) results demonstrate that after laser scribing, the oxygen content decreased greatly (Figure 3C). The oxygen content of CNS is 21 at%, while, the oxygen content of CNS-LSG is around 4 at% (oxygen in  $Na_2CO_3$  is subtracted). The existence of sodium carbonate in CNS-LSG originates from the sodium in CMC binders. The sharp decrease of oxygen content in CNS-LSG compared with CNS demonstrates the successful carbonization of CNS. Analogous results were obtained from the thermogravimetric analysis (TGA) in inert gas, which showed a larger mass loss for the CNS powder (Figure S5, Supporting Information). The C 1s fine spectra of CNS-LSG was fitted by five components (Figure 3D), namely, the  $sp^2$  C=C at 284.4 eV, the  $sp^3$  C—C at 284.8 eV, the C—O at 285.8 eV, C=O at 286.7 eV, and the O—C=O at 288.6 eV. The content of each carbon bonding component is listed in Table S1 in the Supporting Information. The  $sp^2$  carbon content in CNS-LSG is 58.4% much higher than 9.9% of CNS, which, in accordance with Raman and TEM study, demonstrates the graphitization of CNS during the laser scribing process. The high graphitization results in CNS-LSG with a high conductivity of  $33.6 \text{ S cm}^{-1}$  measured by four-probe resistivity measurement. In contrast, CNSs have sheet resistance higher than  $40 \text{ M}\Omega$ . The sharp decrease of  $sp^3$  carbon content after the laser scribing process verifies the laser graphitization mechanism proposed by Kaner and Tour.<sup>[37,38]</sup> The role of photothermal energy may be not so significant in laser

scribing, since the temperature of the laser spot on CNS is only around the melting point of aluminum ( $660^\circ\text{C}$ ) (verified by the slight deformation of the aluminum substrate).

After the laser scribing process, the CNS-LSG films were directly used as electrodes for supercapacitors. However, if aluminum was directly used as substrate, CNS-LSG has low areal capacitance ( $<0.2 \text{ mF cm}^{-2}$ ) and can be only scanned up to  $20 \text{ V s}^{-1}$  (Figure S6A,B, Supporting Information), which could be due to the passive oxide layer which forms during the laser scribing process (demonstrated by the large semicircle of Nyquist plot in the middle frequency range, see Figure S6C, Supporting Information). To avoid the formation of the passive layer,<sup>[39,40]</sup> gold was coated on aluminum foil prior to CNS film coating. To assemble CNS-LSG supercapacitor, two identical CNS-LSG electrodes ( $0.64 \text{ cm}^2$ ) were placed face to face in a 2032 coin cell in commercial supercapacitor electrolyte. Cyclic voltammetry (CV) was used to study the electrochemical behavior of CNS-LSG symmetric supercapacitor in the voltage window of 0–1 V. The cyclic voltammograms of CNS-LSG show rectangular shape from scan rate of  $0.1 \text{ V s}^{-1}$  (Figure 4A) to as high as  $200 \text{ V s}^{-1}$  (Figure 4B), which is much higher than LSG derived from polyimide.<sup>[35]</sup> The high scan rate of  $200 \text{ V s}^{-1}$  indicates that the CNS-LSG supercapacitor can be charged–discharged within 5 ms. Besides, the highest scan rate of  $200 \text{ V s}^{-1}$  for CNS-LSG is three orders of magnitude higher than traditional AC supercapacitor, since AC supercapacitor can be only scanned to  $0.1 \text{ V s}^{-1}$  due to low conductivity of AC and the high diffusion resistance of the pores in AC.<sup>[5,41,42]</sup> Also, the current response of CNS-LSG has almost linear relationship with scan rate up to  $100 \text{ V s}^{-1}$  demonstrating its quasi-ideal capacitive behavior (Figure S7, Supporting Information).

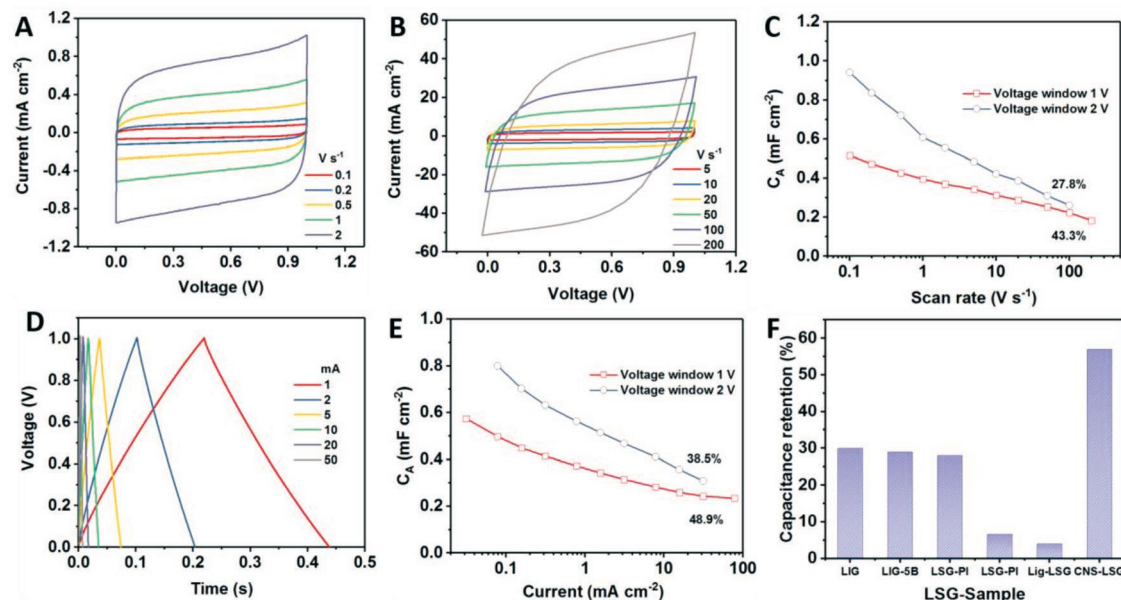


**Figure 4.** A,B) The cyclic voltammograms of CNS-LSG symmetric supercapacitor; C) the dependence of areal capacitance of CNS-LSG symmetric supercapacitor on the scan rates; D) the GCD curves of CNS-LSG symmetric supercapacitor (the surface area of single CNS-LSG electrode is  $0.64 \text{ cm}^2$ ); E) the dependence of areal capacitance on the GCD current densities; and F) the comparison of the rate performances of the CNS-LSG and other LSG with increasing the GCD current density by two orders of magnitude.

Supercapacitors using LSG electrodes and organic electrolytes can be scanned in a wide voltage window of 0–2 V.<sup>[38]</sup> The CNS-LSG electrodes measured in the voltage window of 0–2 V show a higher areal capacitance compared with CNS-LSG electrodes measured in 0–1 V window (Figure S8, Supporting Information). A high scan rate of  $100 \text{ V s}^{-1}$  can be used to scan supercapacitors with CNS-LSG electrodes (Figure S9, Supporting Information). In the voltage window of 0–1 V, CNS-LSG shows a capacitance of  $0.515 \text{ mF cm}^{-2}$ , at scan rate of  $0.1 \text{ V s}^{-1}$ , while 43.3% of the initial capacitance can be retained at a high scan rate of  $100 \text{ V s}^{-1}$  (Figure 4C). In comparison, CNS-LSG electrodes operated at 0–2 V show an areal capacitance of  $0.941 \text{ mF cm}^{-2}$  at  $0.1 \text{ V s}^{-1}$  and 27.8% of the capacitance can be retained at  $100 \text{ V s}^{-1}$  (Figure 4C). In the galvanostatic charge–discharge (GCD) experiments, CNS-LSG electrodes also show high rate performance (Figure S10, Supporting Information and Figure 4D). The CNS-LSG electrode displays perfect triangular shape expected for electric double layer capacitor (EDLC) in the GCD current density range from  $0.078$  to  $78.1 \text{ mA cm}^{-2}$ . When operated at 0–1 V, CNS-LSG electrodes show a high capacitance of  $0.498 \text{ mF cm}^{-2}$  at a current density of  $0.078 \text{ mA cm}^{-2}$ , and 48.9% of the initial capacitance is still retained when the GCD current increased to  $31.2 \text{ mA cm}^{-2}$  (Figure 4E). Similar to the CV test, in the GCD test, the CNS-LSG shows high areal capacitance but low rate capability in the voltage range of 0–2 V. The CNS-LSG electrodes show a capacitance of  $0.800 \text{ mF cm}^{-2}$ , and 38.5% of the capacitance is still retained when the GCD current density increased from  $0.078$  to  $31.2 \text{ mA cm}^{-2}$  (Figure 4E). The rate capability of CNS-LSG is further compared with other LSGs from literature.<sup>[35,43–46]</sup> In fact, CNS-LSG shows the best rate capability among all previously reported LSGs with a high capacitance retention of  $\approx 60\%$ , after increasing the GCD current density by two order of magnitude (Figure 4F). The 4.5% laser power

enables the high performances of the CNS-LSG electrodes. However, if a lower power of 3.5% is used, the highest scan rate of CNS-LSG is limited to  $50 \text{ V s}^{-1}$ , and the capacitance of CNS-LSG is limited to  $0.3 \text{ mF cm}^{-2}$  (Figure S11, Supporting Information). The slow response and low capacitance of CNS-LSG with 3.5% laser power result from the incomplete transformation of CNS located close to the substrate.<sup>[38]</sup>

The high rate capability of CNS-LSG electrodes make it among the best reported supercapacitors from the view point of rate performances. Based on the gravimetric analysis, in the voltage window of 0–1 V, CNS-LSG electrodes show a gravimetric capacitance of  $3.19 \text{ F g}^{-1}$  at current density of  $1 \text{ A g}^{-1}$ . When, GCD current density increases to as high as  $1000 \text{ A g}^{-1}$ , the CNS-LSG electrodes still display a capacitance of  $1.51 \text{ F g}^{-1}$  (Figure S12, Supporting Information) (with a high retention of 47.3%). The CNS-LSG electrodes demonstrate high stability after long-term cycling. After 12 000 GCD cycles, 98.6% of the initial capacitance is retained at a GCD current density of  $1.56 \text{ mA cm}^{-2}$  (Figure S13, Supporting Information).

The high rate capability of CNS-LSG originates from the 3D hierarchical porous structure as well as the high conductivity of graphene, which enables a high-frequency response. The CNS-LSG shows typical Nyquist plot expected for EDLC (Figure 5A), with a small equivalent series resistance of  $0.73 \text{ ohm cm}^{-2}$ . The semicircle in the middle frequency range originates from interfacial phenomenon.<sup>[40]</sup> The semicircle decreased greatly due to the application of a gold intermediate layer, which could be due to prevention of the oxidation of aluminum during the laser scribing process.<sup>[40]</sup> An resistor–capacitor (RC) series circuit model was used to simulate the capacitive and resistive elements in devices using CNS-LSG electrodes. In the RC series model, resistance is obtained from the real impedance and the capacitance is calculated from the

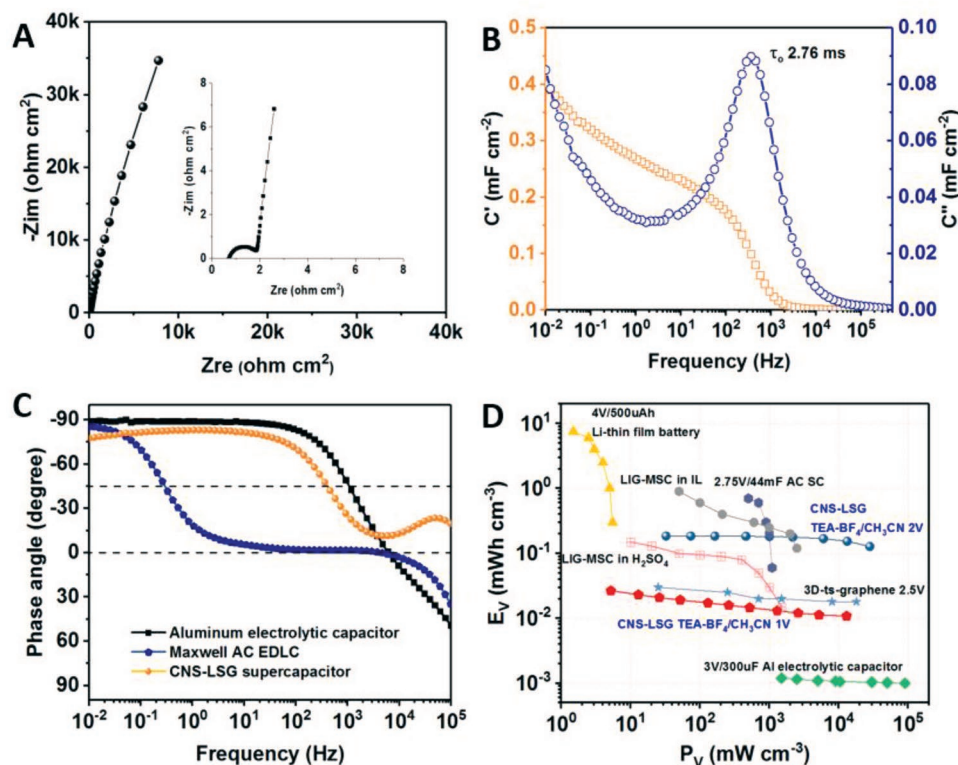


**Figure 5.** A) The Nyquist plot of CNS-LSG, inset is the enlarged high-frequency region; B) the dependence of real and imaginary capacitance of CNS-LSG on frequency; C) the comparison of the frequency response between CNS-LSG, commercial EDLC and aluminum electrolytic capacitor; and D) the comparison of the volumetric Ragone plots of EDLC, Li-thin film battery, aluminum electrolytic capacitor, and LSG electrodes in literatures.

imaginary impedance (Figure S14, Supporting Information).<sup>[9]</sup> At 120 Hz, the resistance is measured to be  $2.5 \text{ ohm cm}^{-2}$ , while the capacitance is measured to be  $0.207 \text{ mF cm}^{-2}$ , with RC constant of  $0.517 \text{ ms}$ . Such a short RC time constant means that the CNS-LSG electrodes could be used in 120 Hz filtering ( $8.3 \text{ ms}$ ) applications.<sup>[47–49]</sup> The real and imaginary capacitance versus frequency curves show the typical behavior for EDLC (Figure 5B), with a relaxation time constant as small as  $2.76 \text{ ms}$ , which is three orders of magnitude smaller than traditional EDLCs.<sup>[50,51]</sup> The frequency response was further compared with commercial EDLC and aluminum electrolytic capacitor (Figure 5C). It can be seen that the commercial EDLC behaves like a capacitor only when the frequency is lower than  $1 \text{ Hz}$ , while electrolytic capacitor behaves like capacitor when frequency is lower than  $5 \text{ kHz}$ . The CNS-LSG also behaves like a capacitor in the same frequency range comparable to the commercial aluminum electrolytic capacitor. Specifically, the frequency of the CNS-LSG electrodes at a phase angle of  $-45^\circ$  is  $402 \text{ Hz}$ , which is much higher than carbon quantum dot derived LSG (3D-ts-graphene) ( $291 \text{ Hz}$ ).<sup>[38]</sup> CNS-LSG electrodes show a high phase angle of  $69^\circ$  at  $120 \text{ Hz}$ . The high frequency response, high phase angle, high capacitance at  $120 \text{ Hz}$  and the easily commercialized characteristic make CNS-LSG electrode suitable for fabricating supercapacitors for frequency-regulation applications. The volumetric power performance of CNS-LSG was further compared with data of various LSG electrodes reported in the literature (Figure 5D). In particular, the CNS-LSG electrodes deliver a maximum volumetric energy density  $0.18 \text{ mWh cm}^{-3}$  (corresponding to

a gravimetric power density  $\approx 2.5 \text{ Wh kg}^{-1}$ ) with an ultrahigh power density of  $28 \text{ W cm}^{-3}$  (corresponding to a gravimetric power density of  $\approx 202 \text{ kW kg}^{-1}$ ), which is 28 times that of commercial AC electrodes, and more than 10 times higher than laser induced graphene electrodes in ion liquid electrolytes,<sup>[35]</sup> more than 18 times higher than electrodes in  $\text{H}_2\text{SO}_4$  electrolyte,<sup>[35]</sup> more than 1.6 times that of 3D-ts-graphene.<sup>[38]</sup> Moreover, at the highest power density, the volumetric energy density of our CNS-LSG electrodes are 7 times higher than the high-power 3D-ts-graphene.<sup>[38]</sup> It needs to be noted that CNS-LSG exhibits the highest power performance among previously reported LSG electrodes derived from polyimides, graphene oxide, lignin, and carbon quantum dots (Table S2, Supporting Information).<sup>[6,43–46,52,53]</sup>

In summary, we propose a new method for the preparation of 3D graphene electrode for ultrahigh-power supercapacitor using laser irradiation. Amorphous carbon nanospheres are transformed into 3D porous graphene electrodes by laser scribing process, leading to better power performance compared to all previous reports on LSG. Our CNS-LSG electrodes show 28-fold higher volumetric power density compared with commercial AC supercapacitor electrodes. Further, the CNS-LSG electrodes shows 7 times higher volumetric energy density compared to LSG electrodes derived from carbon quantum dots (the LSG electrode with the maximum power density reported previously). At the maximum power density of  $1 \text{ W cm}^{-3}$ , the volumetric energy density of CNS-LSG is 6 times higher than the LSG from polyimide. The preparation of CNS-LSG is a green, renewable, and scalable process, using biomass-derived



amorphous CNS. The CNS-LSG electrode can be directly fitted into the commercial organic-electrolyte-based supercapacitor system, showing great potential toward commercialization.

## Experimental Section

**Preparation of CNS-LSG from CNS:** Carbon nanospheres (CNS) used in this work were prepared by hydrothermal reaction. Specifically, 120 mg mL<sup>-1</sup> glucose water solution sealed in teflon-lined stainless steel autoclave was put into air-flow electric oven at 180 °C for 5 h. After cooling down naturally, the brown precipitate was centrifuged and washed with ethanol and deionized water for at least 5 times to get the CNS. After drying at 80 °C overnight, the CNS powder (95%) was grinded and mixed with 5% sodium CMC binder (1.5 wt% water solution) to form a homogeneous slurry and coated with Mayer rod on gold-coated aluminum foils. After drying in a vacuum oven at 70 °C overnight, the CNS film was used to conduct laser scribing process. Typical thickness of the CNS film was around 18 μm (Figure S15, Supporting Information). Laser scribing process was conducted on a commercial CO<sub>2</sub> laser cutting machine (10.6 μm) with a full power of 75 W (Universal X-660 laser cutter platform, Universal, Austria). The laser power was set in the range from 3% to 5.5% and the speed was set at 3.0%. The laser beam was focused at a z distance of 3 mm. After laser scribing, the LSG was directly used as electrodes of supercapacitors without further modification.

**Physical and Electrochemical Characterization of CNS-LSG:** Specific surface area and pore size distribution were evaluated by N<sub>2</sub> adsorption-desorption isotherms measured on a N<sub>2</sub> adsorption/desorption analyzer (ASAP 2420, Micrometrics, USA). Scanning electron microscopy (SEM) images were taken on a scanning electron microscopy (Merlin, ZEISS, Germany). Transmission electron microscopy (TEM) images were taken using transmission electron microscopy (Titan 80-300 ST, FEI, Thermo Fisher Scientific). XRD patterns were collected on a X-ray diffractometer (D8 Advance, Bruker, Germany) with Cu Kα radiation (λ = 1.5406 Å). Raman spectra were collected on a micro-Raman spectrometer (LabRAM ARAMIS, HORIBA Jobin Yvon, Germany) using a cobalt laser (473 nm). The crystal size along the *a* axis was calculated using the Equation (1).

$$L_a = (2.4 \times 10^{-10}) \lambda^4 \left( \frac{I_c}{I_D} \right) \quad (1)$$

TGA was measured using a thermogravimetric analyzer (STA 449F1, NETZSCH, Germany) within the temperature range from 25 to 800 °C at a heating rate 10 °C min<sup>-1</sup> in N<sub>2</sub> atmosphere. XPS analysis was conducted on photoelectron spectrometer (Kratos AXIS Supra, Shimadzu, Japan).

The electrochemical performance of CNS-LSG was evaluated in 2032 coin cell. Two identical CNS-LSG electrodes with geometric size of 0.8 × 0.8 cm were used to assemble symmetric supercapacitors using Celgard 3501 separator. The electrolyte used was 1 M tetraethyl ammonium tetrafluoroborate (TEABF<sub>4</sub>) in acetonitrile (AN). CV, GCD and electrochemical impedance tests were conducted on an electrochemical workstation (VMP3, Biologic, France). Electrochemical impedance spectra were measured at open circuit voltage in the frequency range from 200 kHz to 10 mHz with a sinusoidal voltage amplitude of 10 mV. All measurements were conducted in ambient condition.

The areal capacitances based on the cyclic voltammograms were calculated by Equation (2)

$$C_A = \frac{\int i dV}{2 \times S \times \nu \times \Delta V} \quad (2)$$

where, *S* is the surface area of electrodes (cm<sup>2</sup>), with 0.64 cm<sup>2</sup> for the device configuration of this work. *ν* is the voltage scan rate in V s<sup>-1</sup>, Δ*V* is the voltage range, *i* is the current response in the CV scans. ∫*i* d*V* is the integrated area from CV curve.

The areal capacitances derived from GCD curves were calculated by Equation (3).

$$C_A = \frac{I \Delta t}{S \Delta V} \quad (3)$$

where, *I* is the constant current in GCD measurements. Δ*V* is the voltage change during the discharge process. Δ*V* was calculated using the maximum voltage upon discharge subtract the voltage drop during initial discharge. Δ*t* is the discharge time.

The volumetric energy densities (*E<sub>v</sub>*) and power densities (*P<sub>v</sub>*) were calculated based on Equations (4) and (5).

$$E_v = \frac{1}{2} \times \frac{C_A V^2}{3600 \times 2d} \quad (4)$$

$$P_v = \frac{3600 \times E_v}{\Delta t} \quad (5)$$

where, *d* is the thickness of single electrode in centimeter (15 μm in this work). *C<sub>A</sub>* is the areal capacitance in GCD measurement (in mF cm<sup>-2</sup>). *V* is the working voltage window (V). Δ*t* is the discharge time in second.

For the impedance analysis, the areal real and imaginary capacitances were calculated via Equations (6) and (7).

$$C' = \frac{-Z''}{2\pi f A |Z|^2} \quad (6)$$

$$C'' = \frac{Z'}{2\pi f A |Z|^2} \quad (7)$$

The dependence of capacitance on frequency was calculated via Equation (8).

$$C = \frac{-1}{2\pi f Z''} \quad (8)$$

## Supporting Information

Supporting Information is available from the Wiley Online Library or from the author.

## Acknowledgements

W.Z. and Y.L. contributed equally to this work. Research reported in this publication was supported by King Abdullah University of Science and Technology (KAUST). The authors thank the Advanced Nanofabrication, Imaging and Characterization, and Analytical Chemistry Core Laboratories at KAUST for their excellent support.

## Conflict of Interest

The authors declare no conflict of interest.

## Keywords

carbon nanospheres, high power performance, hydrothermal carbonization, laser scribed graphene, supercapacitors

Received: December 29, 2018  
Published online: January 25, 2019

- [1] D. Qi, Y. Liu, Z. Liu, L. Zhang, X. Chen, *Adv. Mater.* **2017**, 29, 1602802.
- [2] M. Salanne, B. Rotenberg, K. Naoi, K. Kaneko, P. L. Taberna, C. P. Grey, B. Dunn, P. Simon, *Nat. Energy* **2016**, 1, 16070.
- [3] N. Jabeen, A. Hussain, Q. Xia, S. Sun, J. Zhu, H. Xia, *Adv. Mater.* **2017**, 29, 1700804.
- [4] T. Xiong, T. L. Tan, L. Lu, W. S. V. Lee, J. Xue, *Adv. Energy Mater.* **2018**, 8, 1702630.
- [5] Z. Fan, N. Islam, S. B. Bayne, *Nano Energy* **2017**, 39, 306.
- [6] M. F. El-Kady, V. Strong, S. Dubin, R. B. Kaner, *Science* **2012**, 335, 1326.
- [7] Z. H. J. Zhao, Y. Jiang, H. Fan, M. Liu, O. Zhuo, X. Wang, Q. Wu, L. Yang, Y. Ma, *Adv. Mater.* **2017**, 29, 1604569.
- [8] Y. Zhu, S. Murali, M. D. Stoller, K. J. Ganesh, W. Cai, P. J. Ferreira, A. Pirkle, R. M. Wallace, K. A. Cychosz, M. Thommes, D. Su, E. A. Stach, R. S. Ruoff, *Science* **2011**, 332, 1537.
- [9] J. R. Miller, R. A. Outlaw, B. C. Holloway, *Science* **2010**, 329, 1637.
- [10] K. S. Kim, Y. Zhao, H. Jang, S. Y. Lee, J. M. Kim, K. S. Kim, J. H. Ahn, P. Kim, J. Y. Choi, B. H. Hong, *Nature* **2009**, 457, 706.
- [11] X. Li, W. Cai, J. An, S. Kim, J. Nah, D. Yang, R. Piner, A. Velamakanni, I. Jung, E. Tutuc, S. K. Banerjee, L. Colombo, R. S. Ruoff, *Science* **2009**, 324, 1312.
- [12] H. Jin, J. Li, Y. Yuan, J. Wang, J. Lu, S. Wang, *Adv. Energy Mater.* **2018**, 8, 1801007.
- [13] B. Hu, K. Wang, L. Wu, S. H. Yu, M. Antonietti, M. M. Titirici, *Adv. Mater.* **2010**, 22, 813.
- [14] L. Wei, M. Sevilla, A. B. Fuertes, R. Mokaya, G. Yushin, *Adv. Energy Mater.* **2011**, 1, 356.
- [15] M. Sevilla, A. B. Fuertes, *Carbon* **2009**, 47, 2281.
- [16] N. P. Wickramaratne, J. Xu, M. Wang, L. Zhu, L. Dai, M. Jaroniec, *Chem. Mater.* **2014**, 26, 2820.
- [17] L. T. Song, Z. Y. Wu, H. W. Liang, F. Zhou, Z. Y. Yu, L. Xu, Z. Pan, S. H. Yu, *Nano Energy* **2016**, 19, 117.
- [18] J. Zhou, Z. Li, W. Xing, H. Shen, X. Bi, T. Zhu, Z. Qiu, S. Zhuo, *Adv. Funct. Mater.* **2016**, 26, 7955.
- [19] X. Wang, K. Han, D. Qin, Q. Li, C. Wang, C. Niu, L. Mai, *Nanoscale* **2017**, 9, 18216.
- [20] T. B. Shiell, D. G. McCulloch, D. R. McKenzie, M. R. Field, B. Haberl, R. Boehler, B. A. Cook, C. De Tomas, I. Suarez-Martinez, N. A. Marks, J. E. Bradby, *Phys. Rev. Lett.* **2018**, 120, 215701.
- [21] C. Hu, L. Dai, *Adv. Mater.* **2017**, 29, 1604942.
- [22] C. Shi, L. Hu, J. Hou, K. Guo, T. Zhai, H. Li, *Energy Storage Mater.* **2018**, 15, 82.
- [23] J. Huang, B. Zhang, Y. Y. Xie, W. W. K. Lye, Z. L. Xu, S. Abouali, M. Akbari Garakani, J. Q. Huang, T. Y. Zhang, B. Huang, J. K. Kim, *Carbon* **2016**, 100, 329.
- [24] X. Jin, R. He, S. Dai, *Chem. - Eur. J.* **2017**, 23, 11455.
- [25] J. Peng, N. Chen, R. He, Z. Wang, S. Dai, X. Jin, *Angew. Chem., Int. Ed.* **2017**, 56, 1751.
- [26] W. Gao, N. Singh, L. Song, Z. Liu, A. L. M. Reddy, L. Ci, R. Vajtai, Q. Zhang, B. Wei, P. M. Ajayan, *Nat. Nanotechnol.* **2011**, 6, 496.
- [27] Z. Wan, E. W. Streed, M. Lobino, S. Wang, R. T. Sang, I. S. Cole, D. V. Thiel, Q. Li, *Adv. Mater. Technol.* **2018**, 3, 1700315.
- [28] R. Ye, D. K. James, J. M. Tour, *Acc. Chem. Res.* **2018**, 51, 1609.
- [29] M. F. El-Kady, R. B. Kaner, *Nat. Commun.* **2013**, 4, 1475.
- [30] R. Ye, Y. Chyan, J. Zhang, Y. Li, X. Han, C. Kittrell, J. M. Tour, *Adv. Mater.* **2017**, 29, 1702211.
- [31] M. F. El-Kady, R. B. Kaner, *ACS Nano* **2014**, 8, 8725.
- [32] S. Xu, C. Liu, F. Ye, Y. Guo, J. Wiezorek, *Colloids Surf., A* **2017**, 515, 1.
- [33] Z. Wang, H. Ogata, G. J. H. Melvin, M. Obata, S. Morimoto, J. Ortiz-Medina, R. Cruz-Silva, M. Fujishige, K. Takeuchi, H. Muramatsu, T. Y. Kim, Y. A. Kim, T. Hayashi, M. Terrones, Y. Hashimoto, M. Endo, *Carbon* **2017**, 121, 426.
- [34] Z. Q. Hao, J. P. Cao, Y. Wu, X. Y. Zhao, Q. Q. Zhuang, X. Y. Wang, X. Y. Wei, *J. Power Sources* **2017**, 361, 249.
- [35] J. Lin, Z. Peng, Y. Liu, F. Ruiz-Zepeda, R. Ye, E. L. G. Samuel, M. J. Yacamán, B. I. Yakobson, J. M. Tour, *Nat. Commun.* **2014**, 5, 5714.
- [36] J. Zeng, X. Ji, Y. Ma, Z. Zhang, S. Wang, Z. Ren, C. Zhi, J. Yu, *Adv. Mater.* **2018**, 30, 1705380.
- [37] Y. Chyan, R. Ye, Y. Li, S. P. Singh, C. J. Arnusch, J. M. Tour, *ACS Nano* **2018**, 12, 2176.
- [38] V. Strauss, C. Marsh, M. Kowal, M. F. El-Kady, R. B. Kaner, *Adv. Mater.* **2018**, 30, 1704449.
- [39] C. Lei, F. Markoulidis, Z. Ashtaka, C. Lekakou, *Electrochim. Acta* **2013**, 92, 183.
- [40] C. Portet, P. L. Taberna, P. Simon, C. Laberty-Robert, *Electrochim. Acta* **2004**, 49, 905.
- [41] W. Zhang, H. Lin, Z. Lin, J. Yin, H. Lu, D. Liu, M. Zhao, *ChemSusChem* **2015**, 8, 2114.
- [42] W. Zhang, J. Xu, D. Hou, J. Yin, D. Liu, Y. He, H. Lin, *J. Colloid Interface Sci.* **2018**, 530, 338.
- [43] J. Cai, C. Lv, A. Watanabe, *J. Mater. Chem. A* **2016**, 4, 1671.
- [44] J. Cai, C. Lv, A. Watanabe, *Nano Energy* **2016**, 30, 790.
- [45] Z. Peng, R. Ye, J. A. Mann, D. Zakhidov, Y. Li, P. R. Smalley, J. Lin, J. M. Tour, *ACS Nano* **2015**, 9, 5868.
- [46] W. Zhang, Y. Lei, F. Ming, Q. Jiang, P. M. F. J. Costa, H. N. Alshareef, *Adv. Energy Mater.* **2018**, 8, 1801840.
- [47] N. Kurra, M. K. Hota, H. N. Alshareef, *Nano Energy* **2015**, 13, 500.
- [48] N. Kurra, Q. Jiang, A. Syed, C. Xia, H. N. Alshareef, *ACS Appl. Mater. Interfaces* **2016**, 8, 12748.
- [49] Y. Yoo, M.-S. Kim, J.-K. Kim, Y. S. Kim, W. Kim, *J. Mater. Chem. A* **2016**, 4, 5062.
- [50] S. Zhang, N. Pan, *Adv. Energy Mater.* **2015**, 5, 1401401.
- [51] W. Zhang, M. Zhao, R. Liu, X. Wang, H. Lin, *Colloids Surf., A* **2015**, 484, 518.
- [52] F. Wen, C. Hao, J. Xiang, L. Wang, H. Hou, Z. Su, W. Hu, Z. Liu, *Carbon* **2014**, 75, 236.
- [53] X. Yun, Z. Xiong, L. Tu, L. Bai, X. Wang, *Carbon* **2017**, 125, 308.